

# X-ray Microscopy at the Advanced Photon Source

---

IAN McNULTY, BARRY LAI, JÖRG MASER, AND DAVID J. PATERSON

*Argonne National Laboratory*

PAUL EVANS

*University of Wisconsin*

STEVE M. HEALD

*Pacific Northwest National Laboratory*

GENE E. ICE

*Oak Ridge National Laboratory*

ERIC D. ISAACS

*Lucent Corporation*

MARK L. RIVERS AND STEPHEN R. SUTTON

*University of Chicago*

X-ray microscopy has experienced tremendous growth at the Advanced Photon Source (APS) since the synchrotron began operations in late 1996. While this burgeoning productivity could be expected at a third-generation, high-energy storage ring such as the APS, ESRF, or SPring-8, the diversity of techniques (Table 1) and applications that have developed in the intermediate (1–4 keV) and hard (6–30 keV) X-ray energy ranges is impressive. Most of these activities are fueled by undulators combined with X-ray focusing optics, although several heavily subscribed programs are active on bending magnet sources.

Major advances in hard X-ray Fresnel zone plate (ZP) lenses and Kirkpatrick-Baez (KB) mirrors have driven progress in X-ray microscopy at APS. Mirror optics capable of sub-micron focusing and >70% efficiency are used at several beamlines. Efforts are underway to develop KB mirrors at APS with 100 nm resolution using advanced differential deposition and polishing methods. KB mirrors with better than 400 nm resolution made by differential deposition are now in routine use on beamline 34-ID (Figure 1a). In parallel, several beamlines have implemented ZP optics. The latest generation of ZPs in use at APS are made of gold, have outer zone widths of 50–110 nm and thicknesses of 0.4–1.3  $\mu\text{m}$ , with diffraction efficiencies of 10–15% at 2–8 keV energies. To obtain higher efficiency, several identical ZPs are stacked within an optical near-field (Figure 1b).

Fluorescence microscopy, tomography, and microdiffraction are widely used at APS. Applications being pursued at APS Collaborative Access Teams (CATs) and X-ray Operations and Research (XOR) are mostly in the materials, geological, biological/biomedical, and environmental sciences. APS users also take advantage of adjacent optical, atomic force, and electron microscopy facilities.

Scanning fluorescence X-ray microscopy (SFXM) and spatially resolved X-ray absorption near-edge structure (micro-XANES) are among the most active areas at APS. Elemental and chemical state information can now be studied with up to attogram sensitivity. Fluorescence microanalysis experiments in the biological, environmental, and geological sciences, in particular, are thriving. Three-dimensional (3D) imaging by X-ray tomography is also popular among users. New modalities are under development, including phase contrast and fluorescence methods at unprecedented sensitivity [Naghedolfeizi 2003]. Extension of diffraction methods to the micron-scale domain and beyond is one of the most rapidly growing subfields at APS. Microdiffraction utilizing KB and ZP

**Table 1.** X-ray microscopy techniques in use at the Advanced Photon Source

Techniques	APS Beamlines
Scanning transmission X-ray microscopy	2-ID
Scanning fluorescence X-ray microscopy	2-ID, 13-ID, 20-ID
Micro-XANES	2-ID, 13-ID, 20-ID
Micro-EXAFS	10-ID, 13-ID, 20-ID
Microdiffraction	2-ID, 7-ID, 33-ID, 34-ID
Absorption micro/nanotomography	2-BM, 2-ID, 5-BM, 13-BM, 20-ID
Fluorescence microtomography	13-ID
Magnetic microscopy	2-ID, 4-ID
Phase-contrast microscopy	2-ID, 5-BM, 13-BM, 20-ID

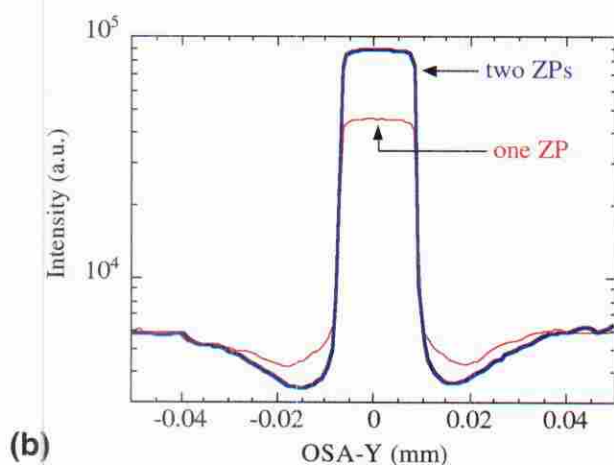


Figure 1: (a) Close-up of polychromatic microdiffraction instrumentation on beamline 34-ID-E. A KB mirror pair is housed in the stainless steel box at right. (b) Relative efficiency of one versus two stacked zone plates, measured with 8 keV X-rays.

optics has become the tool of choice for study of crystal strain, stress, phase, and orientation. Lastly, powerful hybrid techniques have been demonstrated, such as coherent enhancement of the minute diffraction contrast of dislocations in weakly scattering protein crystals [Hu 2001].

#### Scanning fluorescence microscopy and spectro-microscopy

Three scanning X-ray microscopes using ZP optics operate at XOR beamline 2-ID. The 2-ID-D hard X-ray microprobe achieves a spot size of 150 nm. The 2-ID-E microprobe operates in parallel with 2-ID-D at somewhat relaxed resolution (250 nm). The 2-ID-B microprobe offers 60 nm resolution and optimized fluorescence excitation of light elements at intermediate energies. Life science specimens are mainly stud-

ied, where the focus is on mapping and quantification of elements from Na to Zn, and up. The 2-ID-D scanning microscope was used to study small metal complexes such as Zn in bacteria [Labrenz 2000], Pt anticancer agents and Cr carcinogens in single cells [Dillon 2002], and the host-parasite interaction in mycobacterial-infected macrophages. Cell differentiation mediated by metalloproteins, metal accumulation in marine protists, and the biology of TiO<sub>2</sub> nanocomposites in eukaryotes [Paunesku 2003] are being investigated at 2-ID-E. Complementary studies to map low-Z elements are in progress at 2-ID-B.

In Sector 13, GSE-CARS (13-BM and 13-ID) has microscopy efforts on both undulator and bending magnet beamlines in Sector 13. Beamline 13-ID utilizes KB mirrors to produce a 1–3  $\mu\text{m}$  focal spot for X-ray fluorescence microprobe imaging, microspectroscopy, and fluorescence microtomography. Fluorescence is measured with a 16-element Ge detector or a high-resolution wavelength-dispersive spectrometer. Research at GSE-CARS focuses on geochemistry, environmental science, and cosmochemistry. Recent applications include Pb speciation at the biofilm-metal oxide interface [Templeton 2003], identification of chloride complexes in hydrothermal fluid inclusions from an ore-forming region in Australia [Mavrogenes 2002], heterogeneity and speciation of Sr in coral aragonite [Finch 2003], and volatile element contents in interplanetary dust particles [Sutton 2000].

The PNC-CAT (20-ID) undulator beamline is used more than 50% of the time for microbeam and imaging applications. Two sets of KB mirrors provide beam sizes from 1–5  $\mu\text{m}$  to support fluorescence imaging, microspectroscopy, and microdiffraction experiments. The primary application has been to the field of environmental science. Extensive imaging and spectroscopic studies have been made of the fate of Cs, Tc, U and Cr in contaminated sediments from the Hanford Nuclear Reservation. Other studies include As accumulation in plants, As and U in mine tailings, trace elements in meteorites, and trace metals in human liver, lung and breast tissue. The demand for microbeam applications has grown so large that a second KB system is being installed on 20-BM.

#### Scanning transmission microscopy

XOR beamline 2-ID-B performs scanning transmission X-ray microscopy at 1–4 keV energies with simultaneous fluorescence detection. This energy range accesses the K-edges of Na through Ca in addition to the L and M-edges of heavier elements. The 2-ID-B microscope uses fast “on-the-fly” scans and an avalanche photodiode detector to achieve sub-ms dwell times. Applications range from nanotomography of Al and Cu interconnects in integrated circuit chips [Levine 2000] to transmission and fluorescence microscopy of P in mammalian cells [McNulty 2003].

#### Tomography

High throughput microtomography with 1–2  $\mu\text{m}$  resolution is conducted at XOR beamline 2-BM. This system can acquire and reconstruct 720 projections (1024 x 1024 pixels) at 0.25° angular increments in under 5 min. using a dedicated 32-node computer cluster [DeCarlo



2002]. Hundreds of specimens can be studied in a typical 24-hour run. The system is being used in studies of new ceramic thermal barrier coatings for turbine components, anatomy of millimeter-scale organisms, and biomineralization in structures such as sea urchin ossicles (Figure 2).

The DND-CAT bending magnet station 5-BM-C is used for microtomography on a broad range of materials, ranging from 1.2 cm concrete specimens imaged in-situ in a custom load stage at 40 keV, to 2.5 mm wood and polymer samples imaged with 2.4  $\mu\text{m}$  resolution at 7 keV.

The GSE-CARS bending magnet beamline (13-BM) is used for absorption and phase contrast microtomography to image objects up to cm-sized with 2–10  $\mu\text{m}$  resolution. X-ray energies in the range of 15–45 keV are typically used. Recent applications include porosity and permeability of porous media, internal structures of meteorites, dynamic studies of soil drainage and drying, phenocryst size distributions in silicic volcanics, and melt and metal segregation in high-pressure experiments. 13-BM is also used for radiographic imaging in a 250-ton multi-anvil press at pressures up to 28 GPa. Applications include quantitative measurements of deformation under uniaxial stress and locating samples and standards for diffraction measurements.

Both the undulator and bending magnet beamlines at PNC-CAT (20-ID, 20-BM) are used for microtomography at up to 2- $\mu\text{m}$  resolution. Samples range from fossilized bone and teeth to foams and paper.

### Microdiffraction

Hard X-ray microdiffraction activities at the XOR 2-ID-D beamline are supported by a 6-circle Kappa diffractometer integrated with a ZP microprobe and high precision scan stages. A focal spot size of 200–300 nm is typically used. Recent research includes study of the structure of grain boundaries of colossal magnetoresistive films on bicrystal substrates [Soh 2002], evolution of antiferromagnetic domains in Cr [Evans 2002], micro-structures in step-graded SiGe/Si films [Eastman 2002], structure of zirconium alloy oxides, and mapping of strain fields in thin-

film coated substrates due to heteroepitaxial lattice mismatch or deposition stresses.

MHATT-CAT beamline 7-ID focuses mostly on microdiffraction with complementary microfluorescence mapping with a typical resolution of about 1  $\mu\text{m}$ . Microdiffraction is performed with white and monochromatic beams in the 7-ID-B hutch using KB mirrors. Current studies focus on nanoindentation in single crystals. Microdiffraction is also performed in 7-ID-C on a 6-circle Kappa goniometer using either KB or ZP optics. Recent research has focused on the structure of epitaxial films, MEMS, and switching in ferroelectrics.

UNI-CAT beamline 33-ID is a general-purpose monochromatic beamline with microdiffraction capability. A ZP, used to produce a sub-micron X-ray beam, is mounted on an 8-circle Kappa diffractometer with a precision translation stage for measurements in reciprocal space and as a function of position within single crystals.

A dedicated polychromatic X-ray microdiffraction facility operates at a second undulator station at UNI-CAT, 34-ID-E, with the ability to study the phase, morphology, grain orientation, plastic and elastic strain tensor distributions in 3D. The facility uses KB mirrors to focus to 0.5  $\mu\text{m}$  x 0.5  $\mu\text{m}$  and differential aperture microscopy to deconvolute the overlapping Laue patterns generated along an X-ray microbeam as it penetrates into a sample. The resolution along the beam path is ~0.7  $\mu\text{m}$  or better. Although the techniques and instrumentation pioneered on 34-ID (and earlier on a prototype at 7-ID) are still developing rapidly, important science is already emerging.

### Copper speciation in vapor-phase fluid inclusions

Most of the world's Cu and Au ore deposits result from the transport of metals by aqueous solutions at high temperatures and pressures. In some cases, boiling hydrothermal fluids separate into a high-density brine containing metal chloride complexes that form a porphyry deposit and a low-density S-rich vapor that migrates toward the surface before precipitating a high-sulfidation Au(Cu) epithermal deposit. The factors that control metal partitioning between coexisting brine and vapor are the key to understanding the metal distribution in this system. In this study, X-ray fluorescence elemental maps and Cu K-edge XANES spectra were recorded at temperatures up to 400 C for individual vapor and brine phase inclusions from the Mole Granite [Mavrogenes 2002].

Figure 3 shows a room temperature optical image and a Cu X-ray fluorescence map of a vapor-phase fluid inclusion. At room temperature, the low-density vapor-phase inclusion contains a large bubble and a small amount of condensed liquid. The Cu partitioning of interest is between the coexisting phases of the boiling fluid trapped as vapor and brine inclusions, not between the bubble and condensed liquid of the vapor inclusion (the result of cooling). Figure 3b indicates that Cu is concentrated in the vapor-phase inclusion relative to the brine inclusion, in agreement with the results of PIXE analyses. It is also apparent that Cu is homogeneously distributed in the condensed liquid phase of the vapor inclusion and not concentrated in the opaque precipitate, which appears as a cold spot. Cu K-edge XANES spectra identify reversible

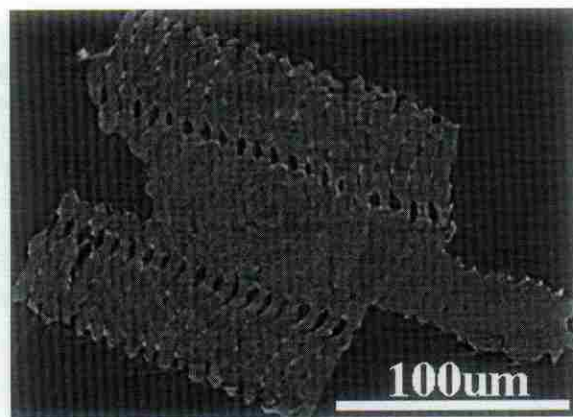
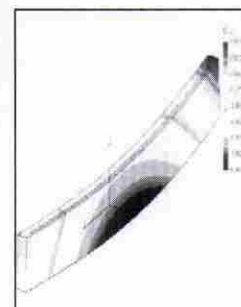
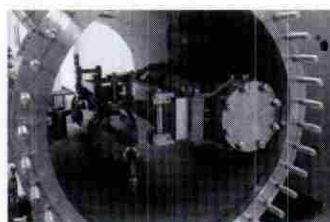


Figure 2: Reconstructed slice of a sea urchin (*Lytechinus variegatus*) tooth fragment. The two rows of dark channels appear not to have been noted previously and may play an important role in nutrient or other transport within the tooth (courtesy S. Stock of Northwestern University).

IRELEC

Beamline Components

## Mirror systems for New generation synchrotron



Easily tunable, precise and reliable shaping,  
designed for automated beamline :

- Mirror-holder, up to 5 axes independent
- Elliptical or cylindrical bender
- KB mirror system for micro-focalisation

**IRELEC, within partnership, provides complete beamline :  
Engineering, components thermo-mechanical analysis, ray-tracing, etc ...**

IRELEC has supplied mirror systems to ESRF, CAMD,  
SSLs, ANKA, etc ...

20 rue du Tour de l'Eau  
38400 ST MARTIN d'HERES - FRANCE  
Tel/fax : 33 4 76 44 12 96 / 33 4 76 63 19 68  
irelec@irelec.fr / www.irelec.com

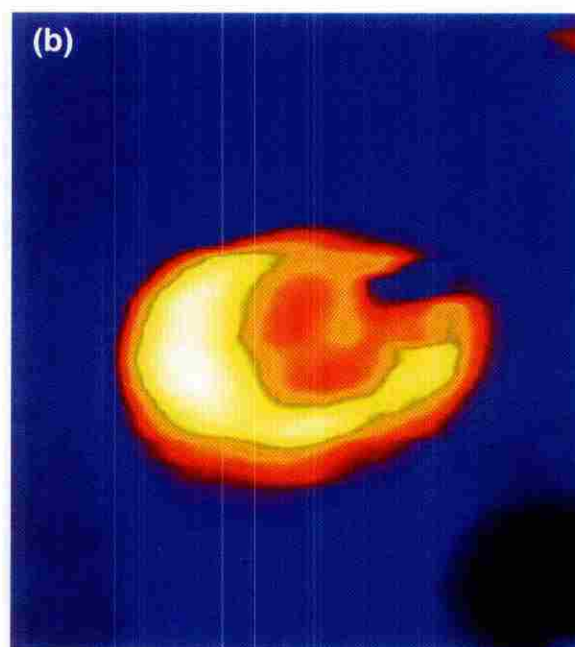
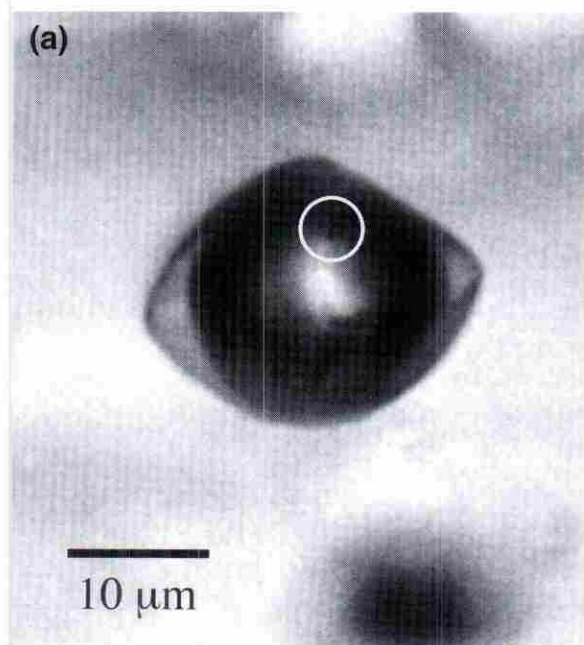


Figure 3: (a) Optical and (b) Cu K $\alpha$  room temperature images of a vapor phase fluid inclusion in quartz. Although single phase when trapped, cooling produces a large shrinkage bubble and a small amount of condensed fluid as shown in (a). The opaque precipitate is circled. The X-ray map indicates that Cu is uniformly distributed in the fluid phase.



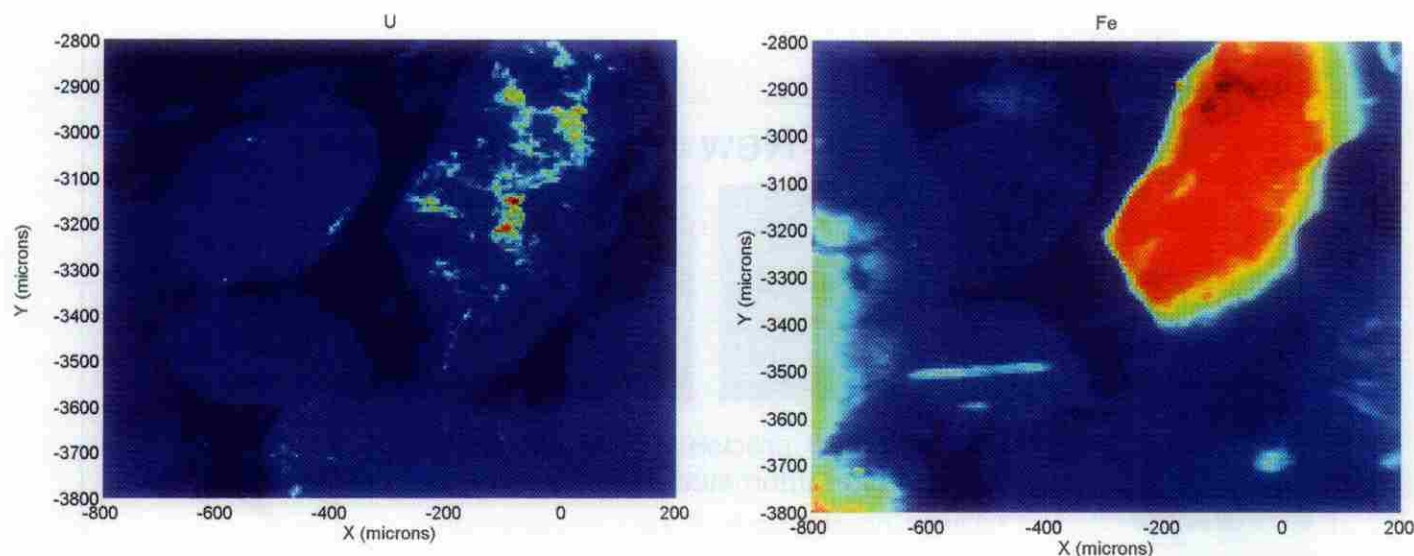


Figure 4: X-ray fluorescence maps for U and Fe from a sediment thin section obtained from under tank BX-102. In these false color images, blue indicates low and red indicates high concentration.

changes in the Cu oxidation state with temperature. This is associated with changes in speciation, which may control the behavior of Cu during the formation of the world's most important Cu ore deposits.

## X-ray microprobe studies of uranium-contaminated sediments

One legacy of the Cold War is a huge inventory of high-level radioactive waste at the Hanford nuclear reservation in the state of Washington. Much of this waste is in the form of aqueous sludge stored in underground tanks. Some of these tanks have leaked, releasing radioactive isotopes such as Cs, Tc and U. In the case of Tank BX-102, several tons of U have been released into the vadose zone. To understand the current and future transport of the released U, it is important to have a detailed microscopic understanding of its disposition in the surrounding sediments. X-ray fluorescence techniques are valuable since the average U concentration is low (<20 ppm by weight) and difficult to find with an electron microscope.

Thin sections of contaminated sediments were examined using the PNC-CAT (20-ID) microprobe, typically with a beam size of 5  $\mu\text{m}$ . Figure 4 shows fluorescence maps for U and Fe from a typical region. A wavelength-dispersive detector was used to isolate the U  $L_{\alpha}$  signal from interfering Sr and Rb  $K_{\alpha}$  fluorescence. It is seen that U-containing particles have precipitated onto the Fe-containing grain. Similar maps can be obtained for elements ranging from K to Sr. Combining these maps with electron microscopy of the same areas, it is possible to correlate the U with various minerals naturally occurring in the sediments. To obtain more information about the U precipitates, bulk and micro-XAFS measurements were made. These determined that the precipitates belong to the uranophane-boltwoodite group of uranyl silicates. The local structure of the U in this group is very similar and a final identification could

not be made by XAFS [Catalano 2002]. A unique identification made using microdiffraction clearly identifies the precipitates as boltwoodite.

Future measurements will look at different sediment layers, the possibility of further mobilization of the U precipitates, and the action of naturally occurring bacteria in generating insoluble U(IV) compounds. These will provide valuable input into developing the most effective cleanup strategies.

## Trace metal content of marine protists

The accumulation of trace metals by planktonic protists influences the growth of primary producers, metal biogeochemical cycling, and metal bioaccumulation in aquatic food chains. Iron is of particular interest as it limits phytoplankton production in large oceanic regions [Coale 1996]. Cellular accumulation of this metal thus influences the contribution of these regions to oceanic C sequestration. Most inferences about oceanic trace metal cycling by protists are from laboratory studies on metal bioaccumulation in monospecific cultures or from metal concentration profiles in oceanic water columns. There are only a few reliable field measurements of trace metal contents of phytoplankton and none of other protists, due to our inability to isolate components of the plankton from complex natural particle assemblages and analyze their metal contents accurately. Bulk size-fractionation techniques cannot distinguish between biotic and abiotic particles or between different species of plankton of similar size, and while they are valuable tools for geochemists, the general nature of the data is less useful for studying the cycling of metals within pelagic plankton communities.

Figure 5 shows an example of a silicoflagellate collected from an Fe-limited region of the Southern Ocean. X-ray fluorescence images and X-ray differential phase contrast were obtained using the XOR 2-

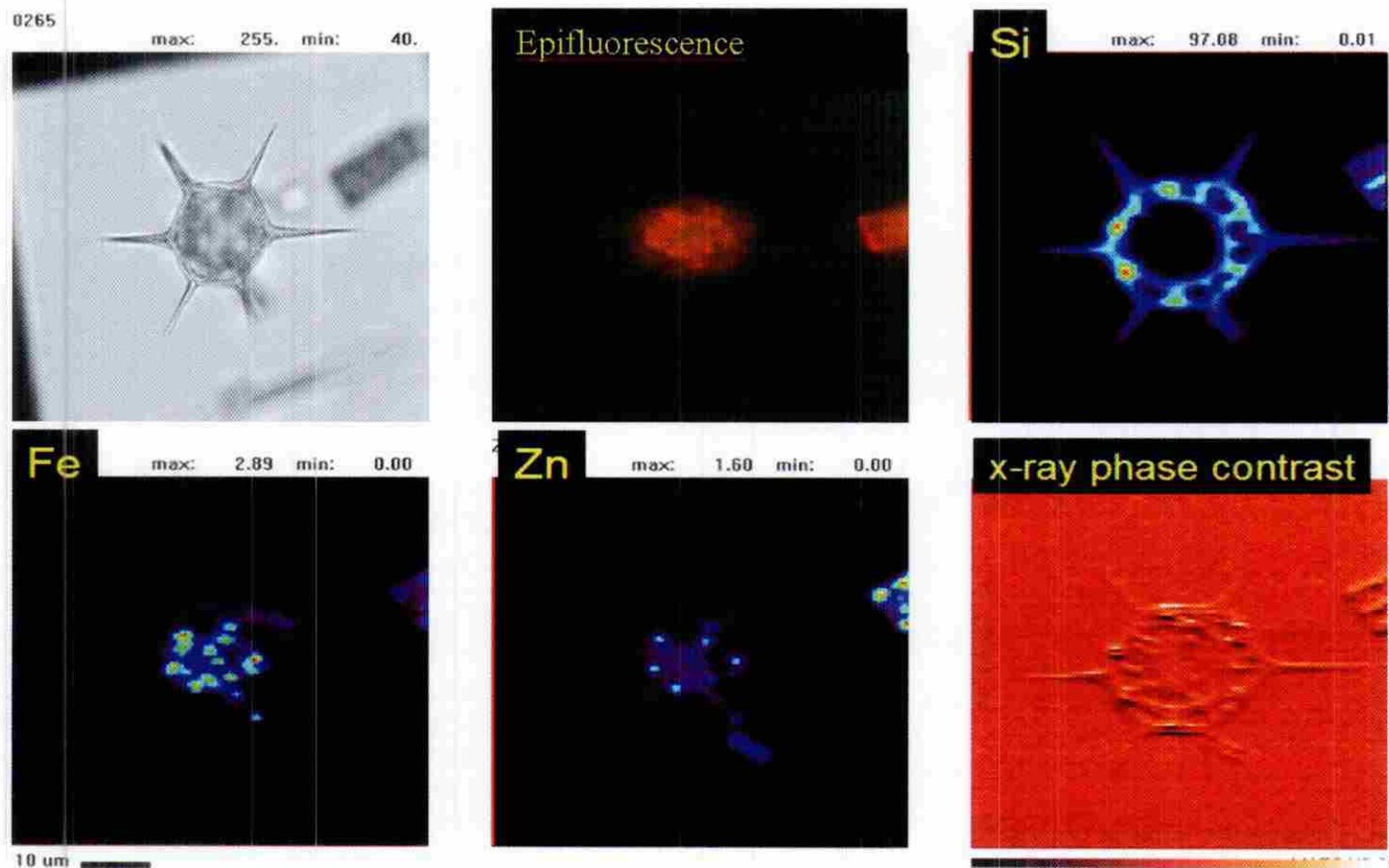


Figure 5: Visible light and epifluorescence micrographs, false-color SFXM element maps, and an X-ray phase contrast image of a silicoflagellate collected from the Southern Ocean (10  $\mu\text{m}$  scale bar).

ID-E microprobe. Fluorescence signatures for different elements are collected in parallel, allowing pixel-by-pixel correlation between major cell constituents such as P, Cl, K, Ca, and trace elements such as Si, Mn, Fe, Cu, Zn. While Si maps onto the opaline shell of the silicoflagellate, Fe and Zn are concentrated in the chloroplast. This work will allow us to reveal trace metal interactions among different members of the same planktonic assemblage to examine metal cycling within the plankton communities.

#### Quantitative phase tomography

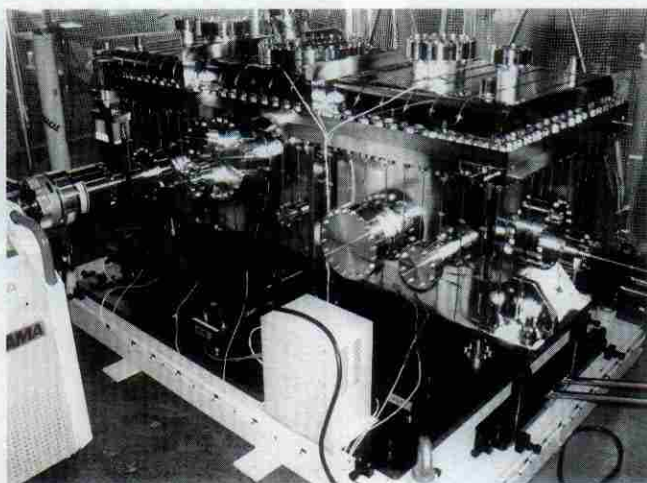
The advent of highly coherent X-ray beams at modern synchrotrons has revolutionized phase-contrast microscopy. A full-field imaging system was recently used to perform tomographic phase imaging at beamline 2-ID-B. In this experiment, a commercial atomic force microscope (AFM) tip was imaged with coherent 1.83-keV X-rays at a resolution of 150 nm, using a ZP lens and a CCD camera. To obtain the phase information, two defocused images were recorded on either side of the in-focus position by translating the ZP along the optical axis. 2D projected phase maps were obtained from the defocus data after cropping and

equilibration to compensate for beam intensity variations. This process was repeated at  $1^\circ$  intervals over a  $180^\circ$  angular range about the sample, then the phase projections were aligned and reconstructed using the filtered back-projection method (Figure 6). The reconstructed 3D resolution is at least 0.9  $\mu\text{m}$ , evidenced by the 6-pixel diameter of the spherical bump (a manufacturing defect) visible in Figures 6b–6f. The reconstructed phase data yielded a measured refractive index decrement of  $\delta = (5.0 \pm 0.5) \times 10^{-5}$ . The calculated value of  $\delta = 5.06 \times 10^{-5}$  at 1.83 keV, based upon the known composition of the AFM tip, is well within experimental error [McMahon 2002].

#### Antiferromagnetic domains in Cr imaged by magnetic microdiffraction

Antiferromagnetic chromium is the quintessential example of a structurally simple metal exhibiting complex magnetism. Electron spins order in a long-period antiferromagnetic density wave and on cooling not only undergo a transition between a disordered, paramagnetic phase and an ordered antiferromagnetic state at the Néel temperature  $T_N$  (311 K), but also display a transition between Néel states of mutually per-





**G-Chamber of SGM for U-10 Beamline  
at Pohang Light Source in Korea  
(Energy Range : 10~1000eV using 6 gratings)**

Supporting cutting-edge science with the best in ultra-high vacuum & precision machining technology.

If you have a good concept that needs to be developed, TOYAMA is the place to come!

We have the technology to turn your ideas into reality.

#### Main Products:

- Beamline Components
- Monochromators
- Mirror Positioners
- Mirror Bending Mechanisms
- UHV Systems
- Standard Feedthroughs

#### Pioneering New Horizons in Science

**TOYAMA Co., Ltd.**

13-16, Hibarigaoka 4-chome, Zama-shi,  
Kanagawa Prefecture, 228-0003, JAPAN  
Tel: +81(46)253-1411 Fax: +81(46)253-1412

E-Mail: salesdept @toyama-jp.com  
Internet Home Page: <http://www.toyama-jp.com>

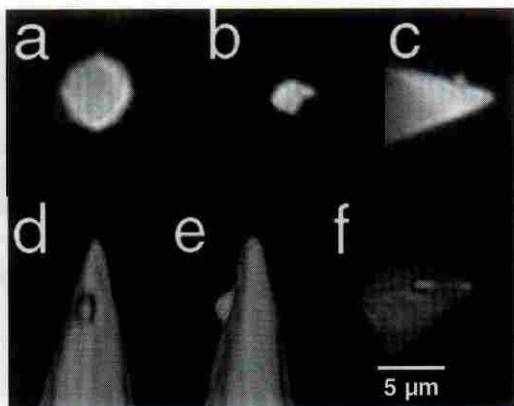


Figure 6: Quantitative 3D reconstructions of the real part of the refractive index of the AFM tip. (a) Horizontal slice through the tip. (b) Horizontal slice including the spherical bump. (c) Vertical slice. (d-f) Volume renderings.

pendicular spin polarizations. Recently, it was discovered that Cr exhibits quantum critical behavior when  $T_N$  is suppressed towards zero degrees with transition metal doping. With no net external magnetic field, antiferromagnets are not only hard to identify, but also extremely difficult to image. The mechanism and dynamics of nucleation and growth of antiferromagnetic domains remained elusive because until now no suitable microscopies have combined sensitivity to antiferromagnetism and spatial resolution.

Individual antiferromagnetic spin density wave domains in a Cr single crystal have been imaged on the 1  $\mu\text{m}$  scale by combining the sensitivity of X-rays to magnetism and X-ray microdiffraction techniques. The cross section for non-resonant magnetic X-ray scattering depends on the antiferromagnetic modulation vector and spin polarization direction thus allowing these quantities to be extracted independently. Figure 7 shows a single spin density wave domain in magnetic X-ray diffraction contrast. The technique was used to show how the broadening of the

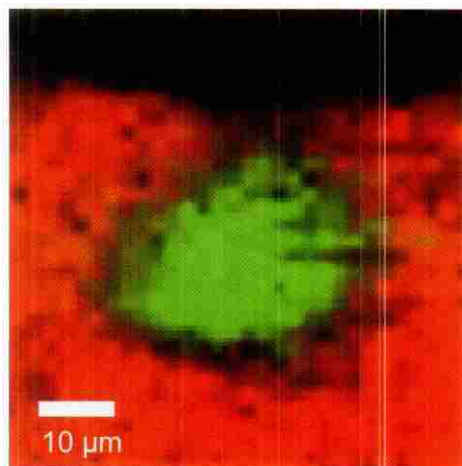


Figure 7: Magnetic diffraction contrast image made by superimposing images of the  $(\delta, 0, 1)$  (red) and  $(0, \delta, 1)$  (green) incommensurate reflections arising from spin density wave domains in a Cr single crystal held at 110 K.

nominally first order "spin-flip" transition at 123 K, at which the spins rotate by  $90^\circ$ , originates at the walls between domains with orthogonal modulation vectors. Magnetic diffraction X-ray microscopy provides a first step towards understanding the relationship of microscopic domains to the bulk properties chromium and promises similar advances in other materials.

### Textured growth of high $T_c$ superconducting films

An early application of microdiffraction facilities at 7-ID and 34-ID has been the study of high  $T_c$  superconductor films. Budai and co-workers measured the orientation of substrate and film grains to understand why certain growth conditions lead to highly oriented films. The results of these measurements (Figure 8) show that growth temperature can drastically affect the growth behavior of buffer and superconducting films. This pioneering work was performed with 2D imaging of the grains in layered materials. The restricted film thickness, unique crystalline phases and distinct defect structure of the layers provide information necessary to localize the sequential structures along the incident beam.

Although these first measurements took advantage of the layered structure of the material to accelerate the data collection, true 3D measurements of mesoscale structure and grain growth are being performed. For example, the 3D X-ray Crystal Microscope at 34-ID can measure grain orientation with two orders of magnitude better angular resolution than electron methods. This makes it highly desirable for testing whether neighbor grains are misoriented to a coincident site lattice. In addition, the plane normal of the grain boundary can be determined to precisely identify the grain boundary type. Such measurements are critical to guide grain-boundary engineering efforts and to understand the mesoscopic structure that results from various processing methods. More ambitious measurements of grain boundary dynamics are underway.

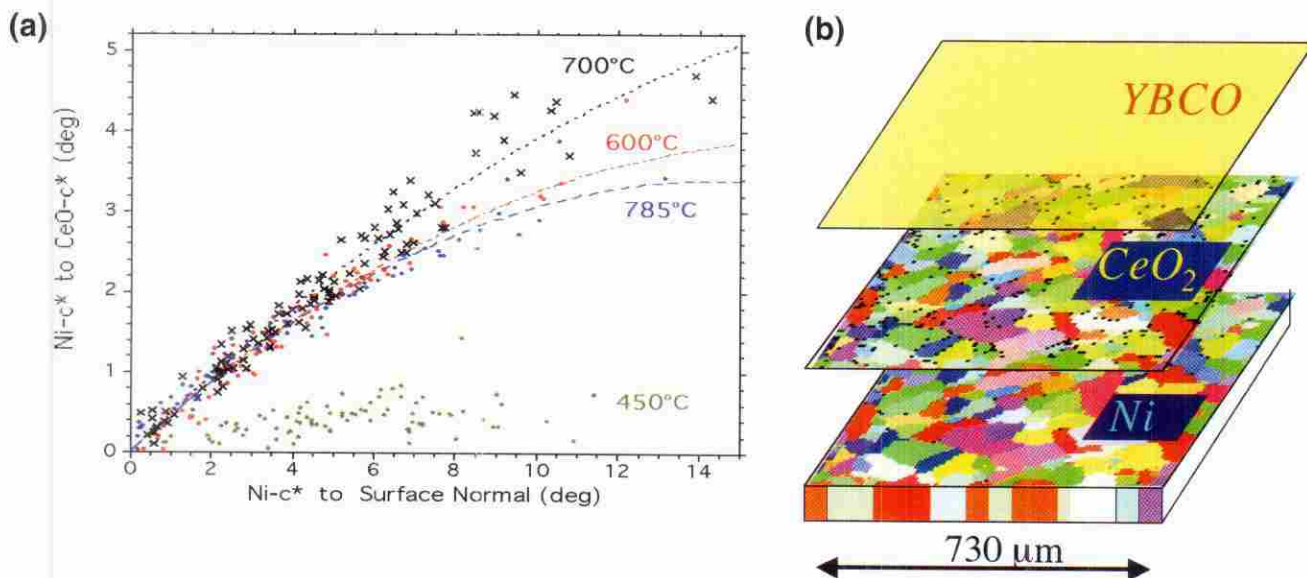


Figure 8: (a) During edge growth, the heteroepitaxial layers align themselves closer to the surface normal than the underlying substrate. (b) The orientations of the layers are closely aligned with the substrate grain orientations.



### Outlook

The number of state-of-the-art applications of X-ray microscopy at APS is expanding rapidly. To name just a few, microfocusing optics have recently been incorporated into inelastic X-ray scattering, coherent scattering, and magnetic imaging experiments. In future, the nanoprobe and other exciting projects will provide unprecedented capabilities for APS users. ■

### Sources Referenced

- K. H. Coale, et al., "A massive phytoplankton bloom induced by an ecosystem-scale iron fertilization experiment in the equatorial Pacific Ocean," *Nature* **383**, 495 (1996).
- J. G. Catalano, J. M. Zachara, and G. E. Brown, Jr., "X-ray Spectroscopic Investigation of the Distribution and Speciation of Uranium in Samples from the BX-102 Borehole," in: Field Investigation Report for Waste Management Area B-BX-BY, *Technical Report RPP-10098*, Rev. 0, Prepared for the Office of River Protection by CH2M Hill Hanford Group, Richland, Washington (2002).
- C. T. Dillon, et al., "Hard x-ray microprobe studies of chromium(VI)-treated V79 Chinese hamster lung cells: intracellular mapping of the biotransformation products of a chromium carcinogen," *J. Biol. Inorg. Chem.* **7**, 640 (2002).
- F. DeCarlo, P. Albee, Y. S. Chu, D. C. Mancini, B. Tieman, and S. Y. Wang, "High-throughput real-time x-ray microtomography at the Advanced Photon Source," *SPIE Proc.* **4503**, 1 (2002).
- D. E. Eastman, et al., "Observation of columnar microstructure in step-graded Si1-xGex/Si films using high-resolution x-ray microdiffraction," *Phys. Rev. Lett* **88**, 156101 (2002).
- P. G. Evans, E. D. Isaacs, G. Aeppli, Z. Cai, B. Lai, "X-ray Microdiffraction Images of Antiferromagnetic Domain Evolution in Chromium," *Science* **295**, 1042 (2002).
- A. A. Finch, N. Allison, S. R. Sutton, and M. Newville, "Strontium in coral aragonite: 1. Characterisation of Sr coordination by EXAFS," *Geochimica et Cosmochimica Acta* **67**, 1189 (2003).
- Z. W. Hu, B. Lai, Y. Chu, Z. Cai, D. C. Mancini, B. R. Thomas, and A. A. Chernov, "Phase sensitive x-ray diffraction imaging of defects in biological macromolecular crystals," *Phys. Rev. Lett.* **87**, 148101 (2001).
- M. Labrenz, et al., "Formation of dphalerite (ZnS) deposits in natural biofilms of sulfate-reducing bacteria," *Science* **290**, 1744 (2000).
- Z. H. Levine, et al., *J. Appl. Phys.* **87**, 4483 (2000).
- J. A. Mavrogenes, A. J. Berry, M. Newville, and S. R. Sutton, "Copper speciation in vapor phase fluid inclusions from the Mole Granite, Australia," *Am. Mineralogist* **87**, 1360 (2002).
- P. J. McMahon, et al., "Quantitative x-ray phase tomography with sub- $\mu$ m resolution," *Opt. Commun.* **217**, 53 (2003).
- I. McNulty, et al., "The 2-ID-B intermediate-energy scanning x-ray microscope at the APS," *J. Phys. IV France* **104**, 11 (2003).
- M. Naghedolfeizi, et al., "X-ray fluorescence microtomography study of trace elements in SiC nuclear fuel shell," *J. Nucl. Mater* **312**, 146 (2003).
- T. Paunesku, et al., *Nature Materials*, **2**, 343 (2003).
- Y.-A. Soh, et al., "Local mapping of strain at grain boundaries in colossal magnetoresistive films using x-ray microdiffraction," *J. Appl. Phys.* **91**, 7742 (2002).
- S. R. Sutton, G. J. Flynn, M. L. Rivers, P. Eng, M. Newville, "X-Ray Fluorescence Microtomography of Individual Interplanetary Dust Particles," Lunar and Planetary Science XXXI, Lunar and Planetary Institute, Houston, Paper 1857 (CD-ROM), (2000).
- A. S. Templeton, T. P. Trainor, A. M. Spormann, M. Newville, S. R. Sutton, A. Dohnalkova, Y. Gorby, and G. E. Brown, Jr., "Sorption vs. biomineralization of Pb by Burkholderia cepacia biofilms," *Environ. Sci. Technol.* **37**, 300 (2003).
- B. S. Twining, et al., "Quantifying trace elements in individual aquatic protist cells with a synchrotron x-ray fluorescence microprobe," submitted for publication.

## Coming soon to Synchrotron Radiation News . . .

*Synchrotron Radiation News* is celebrating its sixteenth year of publication by focusing on the newest trends, research, and equipment in the field. Our in-depth coverage will include updates from new facilities, reports from important conferences, and reviews of synchrotron research at work in many different areas.

Don't miss a single issue! If you are not yet receiving your own copy of *Synchrotron Radiation News*, please fill out the subscription card inside this issue, or contact:

Circulation and Subscriptions, Taylor & Francis Inc.  
325 Chestnut Street, 8th floor  
Philadelphia, PA 19106, USA  
Tel: +1-215-625-8900 • Fax: +1-215-625-8914  
Web: [www.taylorandfrancis.com](http://www.taylorandfrancis.com)